Lab on a Chip

PAPER

View Article Online
View Journal | View Issue

Cite this: *Lab Chip*, 2017, **17**, 2831

Holographic microscope slide in a spatio-temporal imaging modality for reliable 3D cell counting†

Biagio Mandracchia, ‡*[a] Vittorio Bianco,‡[a] Zhe Wang,[ab] Martina Mugnano,[a] Alessia Bramanti,[ac] Melania Paturzo[a] and Pietro Ferraro [a]

Received 15th April 2017,
Accepted 11th July 2017

DOI: 10.1039/c7lc00414a

rsc.li/loc

In the current trend of miniaturization and simplification of imaging flow cytometry, Lab-on-a-Chip (LoC) microfluidic devices represent an innovative and cost-effective solution. In this framework, we propose for the first time a novel platform based on the compactness of a holographic microscope slide (HMS) in combination with the new computational features of space-time digital holography (STDH) that uses a 1D linear sensor array (LSA) instead of 2D CCD or CMOS cameras to respond to real diagnostic needs. In this LoC platform, computational methods, holography, and microfluidics are intertwined in order to provide an imaging system with a reduced amount of optical components and capability to achieve reliable cell counting even in the absence of very accurate flow control. STDH exploits the sample motion into the microfluidic channel to obtain an unlimited field-of-view along the flow direction, independent of the magnification factor. Furthermore, numerical refocusing typical of a holographic modality allows imaging and visualization of the entire volume of the channel, thus avoiding loss of information due to the limited depth of focus of standard microscopes. Consequently, we believe that this platform could open new perspectives for enhancing the throughput by 3D volumetric imaging.

Introduction

Lab-on-a-Chip devices emulate the functionalities of a modern analysis laboratory as a compact system, which is realizable at contained costs.[1] LoC microscopy systems are generally desired to provide quantitative measurements and high-throughput data collection.[2–8] To provide imaging with a reduced amount of optical components, LoC devices often exploit the flow of samples in a microfluidic environment. This has led to the development of smartly engineered devices where accurate microfluidic control provides imaging with novel features and improved capabilities.[9–12]

Digital holography (DH) microscopy matches well with the LoC requirements and has been used in this framework to study cell mechanics and life cycles with quantitative assessments,[13–15] for 3D tracking,[16] and to investigate cell adhesion on biocompatible substrates.[17]

Holographic techniques can yield a very high throughput, thanks to their *a posteriori* refocusing capability. This allows recovering out-of-focus information that in standard bright field microscopy is usually lost. To date, the most common approaches for phase retrieval in LoC devices have relied on digital in-line holography (DILH).[18,19] In any strategy based on DILH, proper iterative algorithms are used to solve the twin-image problem, and convergence to a solution is not always guaranteed.[20] Configurations for phase-contrast imaging by means of the transport-of-intensity equation (TIE) have been also demonstrated; however, they turn out to be not quantitative in a number of practical situations where cell alignment is unfeasible.[18,21,22] To get rid of the shortcomings derived from twin-image superposition, the off-axis DH configuration is usually the best choice. Nevertheless, compact set-ups for applications in microfluidics have appeared only recently.[23]

While all the aforementioned techniques require 2D CCD or CMOS cameras, space-time digital holography (STDH) is a coherent imaging technique for microfluidic environments that records the full flow using a linear sensor array (LSA) instead[5,8] (see Fig. 1a and b). The linear array is placed orthogonally to the channel, as shown in Fig. 1d, so that all the flowing objects passing in correspondence with that section of the channel will be recorded. In this way, the spatial information along the flow direction can be recovered along the temporal dimension.[5,8] This implies a substantially unlimited

[a] *Institute of Applied Sciences and Intelligent Systems—Italian National Research Council (ISASI-CNR), Via Campi Flegrei 34, 80078 Pozzuoli (NA), Italy. E-mail: b.mandracchia@isasi.cnr.it*
[b] *College of Applied Sciences, Beijing University of Technology, Beijing 100124, China*
[c] *IRCCS Centro Neurolesi "Bonino Pulejo", Messina, Italy*

† Electronic supplementary information (ESI) available. See DOI: 10.1039/c7lc00414a

‡ These authors equally contributed to the present work.

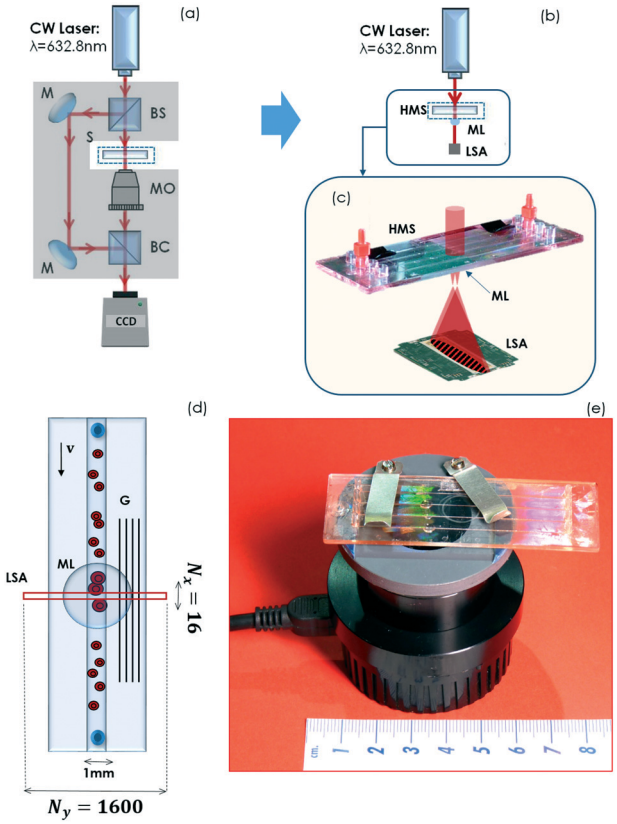

Fig. 1 Sketch of the pocket holographic microscopy module. (a) Classical Mach–Zehnder interferometer. M: mirror; BS: beam-splitter; S: microscope slide; MO: microscope objective; BC: beam-combiner. Schematic representation of the chip-based holographic microscope: (b and c) side view, (d) top view. HMS: holographic microscope slide; ML: micro-lens; LSA: linear sensor array; G: grating. (e) Picture of the device.

field-of-view (FOV) because all imaging data are permanently recorded and stored in just a single continuous digital hologram. However, in such holograms, temporal information and spatial information are tightly related so that the images' reliability depends on the control of flow velocity.

This aspect is especially critical for volumetric imaging inside a microfluidic channel, where a velocity distribution unavoidably occurs, *i.e.* the particles' speed is related to their position inside the liquid volume.[24]

The working principle of STDH has been shown in ref. 8, where quantitative, label-free phase-contrast mapping of samples using test and model organisms has been demonstrated. However, the issue of non-ideal flow established inside the channel has not been tackled yet. In order to apply STDH to microfluidics experiments involving velocity distributions that could adversely affect image reconstruction by spatio-temporal scanning STDH,[5,8] this issue needs to be addressed and solved.

In this work, we propose an approach that provides a stable solution for the full exploitation of STDH in the framework of lab-on-a-chip biomedical applications.

Here, we present a portable STDH platform. In particular, we have developed a novel processing approach to record and process holograms. This approach, combined with the compactness of a holographic microscope slide (HMS), makes it possible to achieve reliable and high-throughput cell counting and tracking by the use of the STDH technique. We show that, using a custom numerical computation approach, the platform achieves robustness against non-ideal flow conditions and the expected distribution of sample velocities inside the channel volume. We tested the platform and the novel algorithms in a case matching real diagnostic needs, *i.e.* high-throughput counting by direct imaging and 3D tracking of red blood cells (RBCs) flowing inside a microfluidic channel under non-ideal fluid control. The effectiveness of the HMS combined with the novel STDH algorithm suite is hereafter demonstrated, paving the way for the use of the proposed platform for real high-throughput diagnostics.

Working principle

In DH, a pattern of interference has to be captured between the wavefront passing through the sample, *i.e.* the object beam, and a reference wave obtained from the same coherent source and directly impinging on the recording device. Fig. 1(a) shows a typical scheme implementing a Mach–Zehnder interferometer in the transmission configuration. Obtaining the object and the reference arms of the interferometer involves the use of a set of optical components, *i.e.* beam splitters, beam combiners, mirrors and at least one microscope objective. The beam emitted by the laser has to be first split and then recombined, which requires fine alignment and can make the set-up bulky. In contrast, the HMS module introduced in ref. 23 greatly simplifies the experimental set-up as no macroscopic optical components are required anymore. As shown in Fig. 1(b), both the external interferometer and the microscope objective are embedded in the chip itself, thus realizing a compact on-chip DH microscope.

Fig. 1(c and d) show a schematic view of the engineered LoC for embedded spatio-temporal scanning holography. A picture of the real system is shown in Fig. 1(e). The interference process is driven by a polymer grating (G) written onto the chip surface with the grating lines parallel to the microfluidic channel. The grating period was set to g_P = 1.67 μm. Once the wavefront emitted by the laser (λ = 632.8 nm) encounters the chip surface, a portion of the beam propagates unaltered toward the objects flowing inside the channel and acquires sample information. Afterwards, light passes through a polymer lens directly printed onto the chip. The lens is printed by means of the forward pyro-electrohydrodynamics method.[25] The lens has a diameter of 2 mm and a focal length of 3 mm. Its numerical aperture, NA, is 0.33 and the estimated depth of focus is 2.9 μm.

At the same time, a portion of the beam that falls out of the microfluidic channel is diffracted by the grating surface and multiple diffraction orders arise at different angles with respect to the object beam. The chip is designed to produce off-axis interference between the first order of diffraction and the object beam. The advantage of the off-axis configuration is that the refocusing process can be carried out by reconstruction methods

conventionally adopted in DH. This is useful for volumetric imaging, where multiple objects are displaced at different positions inside the liquid volume, because out-of-focus objects can be retrieved without the need for iterative algorithms.[20]

Let $O(x,y)$ and $R(x,y)$ be the object and the reference wave in the recording plane (x, y) and let $\sum = \{H_1,...,H_{N_t}\}$ be the set of hologram stripes recorded using the LSA, with a frame rate F_R, while letting the samples flow along the channel at a constant velocity v. In each hologram of the sequence, the complex object distribution is contained as the amplitude and phase modulation of interference fringes with a spacing period p, determined by the angle θ_1 between the object and the reference wave:

$$H_i = |O + R|^2 = (|R|^2 + |O|^2) + R^*O + RO^* = H_i^0 + H_i^{+1} + H_i^{-1}, \quad i = 1,\ldots,N_t \qquad (1)$$

where we indicated the conjugate operator with * and the apices 0, +1, and −1 denote the three orders of diffraction. These are well separated in the Fourier domain due to the off-axis spatial carrier, so that the order of interest, H_i^{+1}, could be in principle extracted for each stripe.

Here, we exploit the sample movement inside the channel to acquire a set of signals using a linear sensor array (LSA) with the number of pixels being $(N_x, N_y) = (16, 1600)$. This assures compactness and a much higher frame rate at contained costs.

Indeed, even though a CMOS area scan camera can reach frame rates higher than 300 Hz, standard models seldom exceed 60 Hz.[26] On the other hand, the scan speed of a CCD LSA is in the range of 400–900 Hz and can be higher than 60 kHz for its CMOS counterparts.[27]

Instead of working on each single hologram, STDH is performed by extracting one single line, $x = x_0$, from each frame to obtain a synthetic hologram representation in the

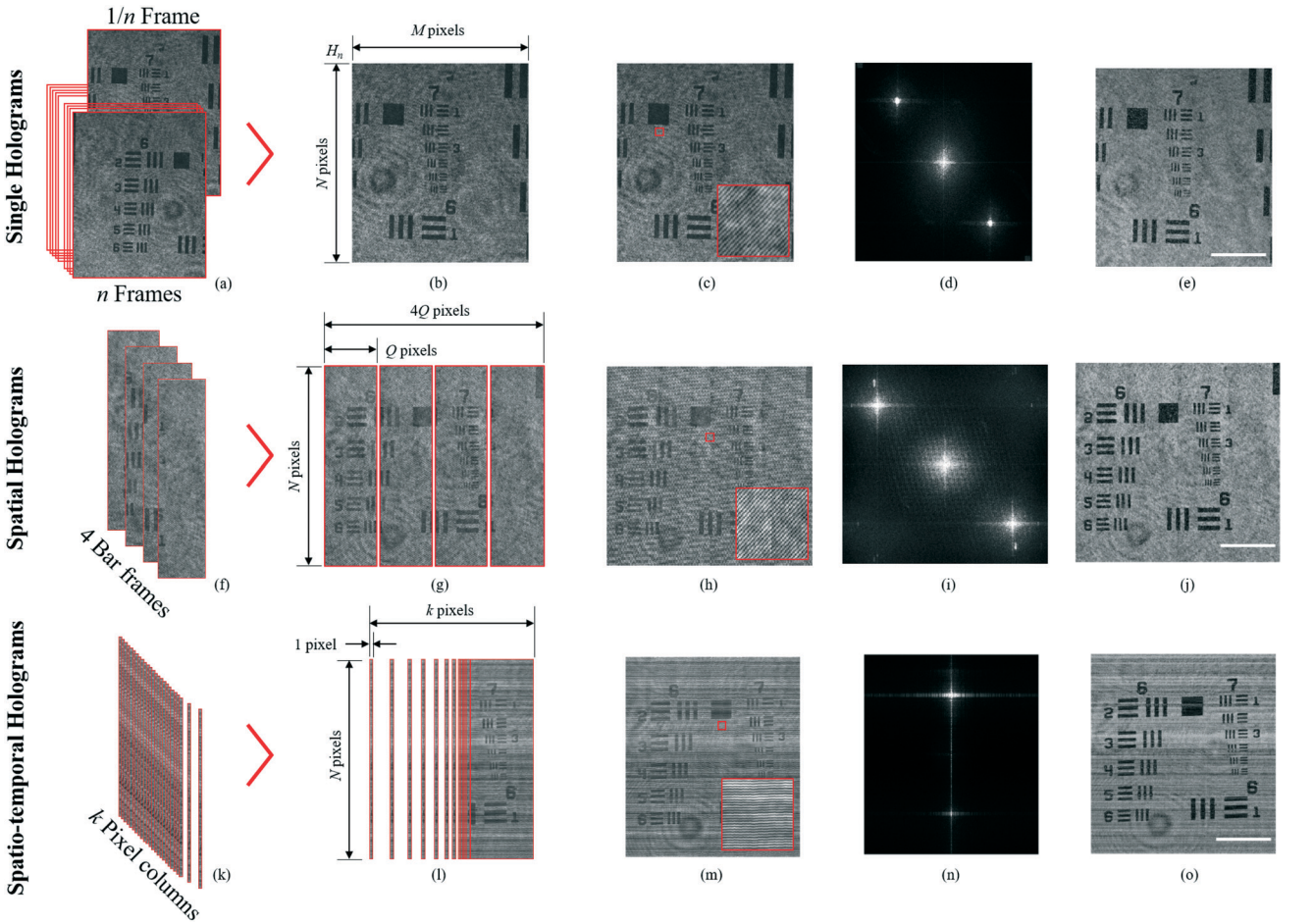

Fig. 2 Comparison of different types of holograms. A USAF test resolution target is moved along the x direction and DH time sequences are captured. (Top row) Single spatial holograms: (a) a time sequence of spatial holograms. (b) One single hologram extracted from the sequence in (a) and its size. (c) The spatial hologram in (b) with interference fringes highlighted in the inset. (d) Fourier amplitude spectrum of the hologram in (b). (e) Amplitude reconstruction resulting from the single spatial hologram in (b). (Middle row) Spatial hologram stripes: (f) a time sequence of four striped holograms. (g) Stitched hologram obtained from the sequence in (f) and its size. (h) Stitched hologram obtained from the sequence in (f) and interference fringes highlighted in the inset. (i) Stitched Fourier amplitude spectrum. (j) Amplitude reconstruction resulting from the stitched hologram in (g). (Bottom row) Spatio-temporal hologram: (k) pixel columns to form the spatio-temporal hologram. (l) STDH synthesized from the sequence in (k) and its size. (m) STDH synthesized from the sequence in (k) and projected interference fringes highlighted in the inset. (n) Fourier amplitude spectrum of the STDH in (m). (o) Amplitude reconstruction resulting from the STDH in (m). Scale bars: 100 μm.

hybrid space-time domain, $H_S(y, t; x = x_0)$.[5,8] STDH has been demonstrated to possess all the capabilities of classical DH mapped in the 2D spatial domain, but with some intrinsic advantageous features. The generation of synthetic holograms is depicted in Fig. 2, along with a comparison with other stitching methods that can be used to extend the FoV.

The STDH synthesis process involves fringe projection, so that the object always modulates horizontal fringes with spacing $p' = p/\cos\alpha$, where α denotes the angle formed by the hologram fringes with the x axis. If the sample speed is properly matched to the frame rate,[8] STDH provides a single hologram of the sample with an unlimited FoV along the scan direction, independent of the magnification factor. In-focus images can then be obtained at any depth by numerically refocusing the recorded digital hologram. In other words, the entire synthetic representation of the sequence can be propagated along the optical axis in one single reconstruction, avoiding cumbersome hologram stitching and, thus, providing the refocused complex image in the hybrid's best focus domain (y_F, t):

$$C(y_F, t; z) = P_z\{H_S^{+1}(y, t; x = x_0)\} \quad (2)$$

where H_S^{+1} denotes STDH after extracting the diffraction order of interest, and $P_z\{...\}$ is the propagator operator[28] performing refocusing at distance z. Propagation at various distances results in a stack of complex images where different objects can be imaged in sharp focus. The joint action of unlimited FoV imaging in a coherent scanning modality and flexible numerical refocusing makes the proposed optical module an extremely high-throughput microscope.

In STDH imaging, nonetheless, an important requirement is the temporal stability of the interference fringes. Systems for vibration isolation are generally needed in order to guarantee stable fringes during the recording time. We overcome this limitation using a HMS. This, with its quasi-common-path wavefront division scheme, allows a certain degree of tolerance to vibrations, so that the system can be brought out of the lab. Temporary instabilities would affect reference and object beams in the same way, leaving the optical path difference between the two beams almost unaltered and assuring stable fringe patterns over time.

Results

We have used our device to count and track RBCs in 3D by volumetric imaging. Above all, we aimed to show the capability of the proposed chip design to make the compact optofluidic microscope a very high-throughput diagnostic device by capturing all RBCs that travel along the microfluidic channel even if they flow at different speeds.

We let the RBCs flow inside the microfluidic channel at a controlled constant velocity ($\bar{v}$ = 109.5 μm s^{-1}) by means of a syringe pump (Harvard apparatus). The dimensions of the microfluidic channel were 58.5 mm × 1 mm × 200 μm. The hologram sequence was recorded using the LSA with N_x = 16 and N_y = 1600 square pixels with pitch $\Delta x = \Delta y$ = 4.5 μm. The magnification factor provided by the polymer microlens was M = 18, so that the limited FoV of each recorded stripe hologram was $\mathrm{FoV}_x = \frac{N_x \Delta x}{M} = 4$ μm along the flow direction and $\mathrm{FoV}_y = \frac{N_y \Delta y}{M} = 400$ μm along the y axis. A total of N_t = 25.2 × 10^4 frames was recorded at a frame rate F_R = 438 Hz so that the overall acquisition time was T = 575.3 s.

In STDH, the maximum obtainable FoV is in principle infinite along the flow direction. With these settings, the STDH hybrid representation allows the change from a total number of pixels in the spatial domain, $N_{space} = N_x \times N_y = 2.56 \times 10^3$, to a greatly larger number of pixels in the hybrid domain, $N_{space\text{-}time} = N_y \times N_t = 4.03 \times 10^8$. If a longer T is acceptable, this number can be indefinitely increased without involving further processing steps (one single STDH reconstruction through the $P_z\{...\}$ operator is required). To save space, in the following discussion only a portion of the very long STDH rectangular matrix will be shown, corresponding to the subset of $N_{space\text{-}time} = 3.84 \times 10^7$ pixels.

Starting from the $\sum$ stack, we extracted the median line, x = 8, and we built the STDH of the entire experiment. A part of the hybrid STDH representation is shown in Fig. 3(a), where horizontal fringes code the diffraction of multiple RBCs displaced in different positions inside the liquid volume. The STDH is a very wide FoV synthetic hologram. Nevertheless, the FoV extension is not obtained, sacrificing the magnification. Indeed, although the out-of-focus RBCs seem to be not very visible in the matrix in Fig. 3(a), the STDH contains enough information to resolve each sample and its own diffraction pattern. This is clear in the 2× zoomed in view in Fig. 3(b) and even more in the 8× zoomed in view in Fig. 3(c). The enlarged areas correspond to the segments of the STDH highlighted by colored boxes in Fig. 3(a). The well recognizable diffraction pattern modulating the horizontal spatial carrier in Fig. 3(c) makes the possibility to propagate the STDH apparent to refocus each sample. Different from inline DH approaches, this is feasible without iterative processing, which aimed to extract the first order of diffraction from the twin image and the zeroth order. In our scheme, the orders of diffraction are spatially separated in the Fourier domain as an effect of the spatial carrier, so that H_S^{+1} can be trivially obtained from H_S.

Well-sampled RBCs, *i.e.* the cells moving at the nominal velocity $\bar{v}$, can be easily located by thresholding the reconstructed holograms. Under real flow conditions, however, a velocity distribution is established inside the channel. This depends on the sample position inside the volume and the distance from the channel walls. We can assume that the well-sampled cells are the ones flowing at the nominal velocity value, $\bar{v}$, while faster cells moving at $v > \bar{v}$ are undersampled and will look squeezed.

Different from the well-sampled RBCs showing almost circular diffraction patterns, undersampled RBCs are represented in the STDH as ellipses with different eccentricity factors. In the planes where these are defocused, a weak diffraction pattern is

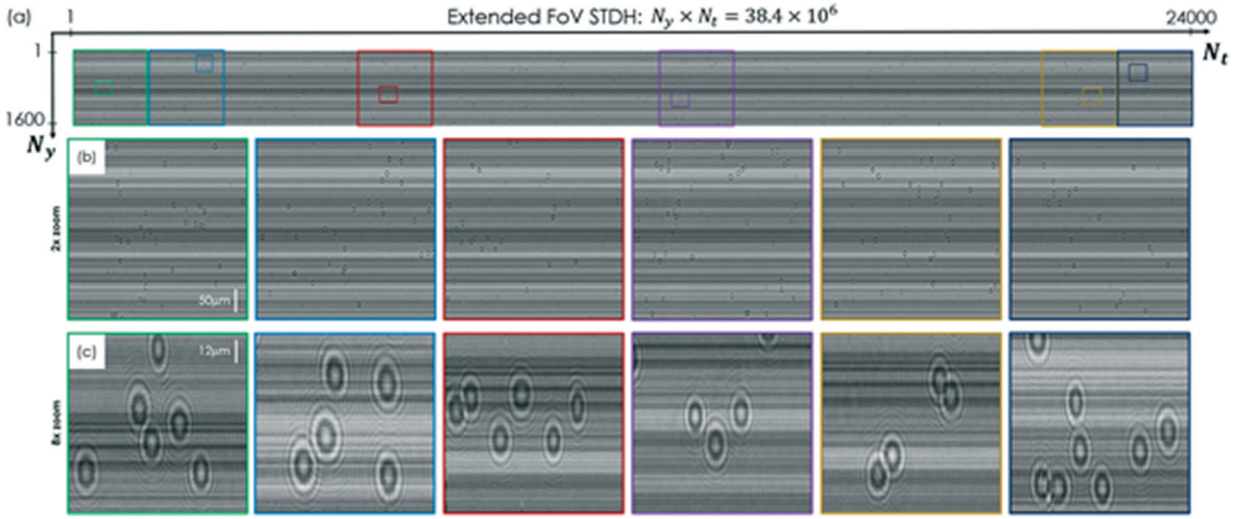

Fig. 3 Spatio-temporal hologram of RBCs flowing in the microfluidic channel. (a) A segment of the entire STDH obtained from $\sum$, corresponding to an extended FoV, hybrid DH representation of the samples. N_y = 1600; N_t = 2.4 × 10^4. (b and c) Enlarged details corresponding to the colored boxes in (a), zoomed in with (b) a 2× factor and (c) an 8× factor. This figure shows that the cells' diffraction pattern is properly captured, because in STDH, the FoV extension is obtained with no resolution loss.

exhibited, so that conventional thresholding could not be applied, as it would fail in most of the cases. Moreover, such an elliptical undersampled pattern does not propagate properly, and the signal associated with these cells in their own best-focus planes is not a sharp spot but rather a cross-like shaped pattern. For these reasons, a different strategy is necessary to achieve more effective cell counting and tracking.

To account for speed distribution, we adopted a deconvolution approach. The algorithm first operates on the STDH and classifies the RBC patterns according to their eccentricity factors assuming that the null eccentricity value corresponds to a circular, well-sampled RBC. Then, deconvolution between the STDH and each different ellipse is performed. Thus sorting, locating and counting of all the differently shaped patterns are feasible. Consequently, undersampled RBCs are not missed and all the objects can be sorted on the eccentricity basis that, in turn, is related to the object's velocity. More details on the adopted procedure are reported in the ESI.†

In Fig. 4, the cells flowing at different speeds are sorted and marked with different colors. The arrows of different lengths indicate the cells moving in different velocity ranges. Most of the cells appear to be well-sampled. However, the amount of not properly sampled RBCs is estimated to be around 17% of the total sample (see the ESI†). Although proper imaging of these cells is not guaranteed (the cell diffraction pattern is properly sampled only along the y coordinate), segmentation based on deconvolution of elliptical shapes can be applied, which is fast and effective in isolating the undersampled RBCs and retrieving the corresponding centroids. The velocity distribution inside the channel and the consequent undersampling of the RBCs do not affect the final counting performance, thus making the proposed approach very robust.

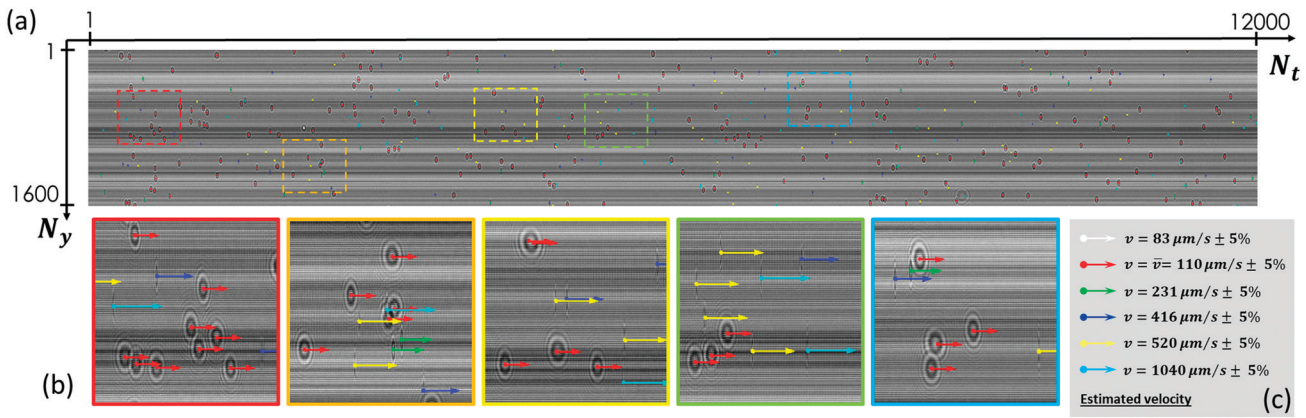

Fig. 4 Velocity distribution inside the channel. (a) For each particle, we determine the eccentricity and, consequently, estimate the velocity. (b) Zoomed in images of the framed areas in (a). The colored arrows represent the velocity evaluated for each particle they are attached to. The values are reported in the legend. (c) The eccentricity distribution inside the channel does not peak around a central value, showing a non-ideal experimental condition. Scale bar: 12 μm.

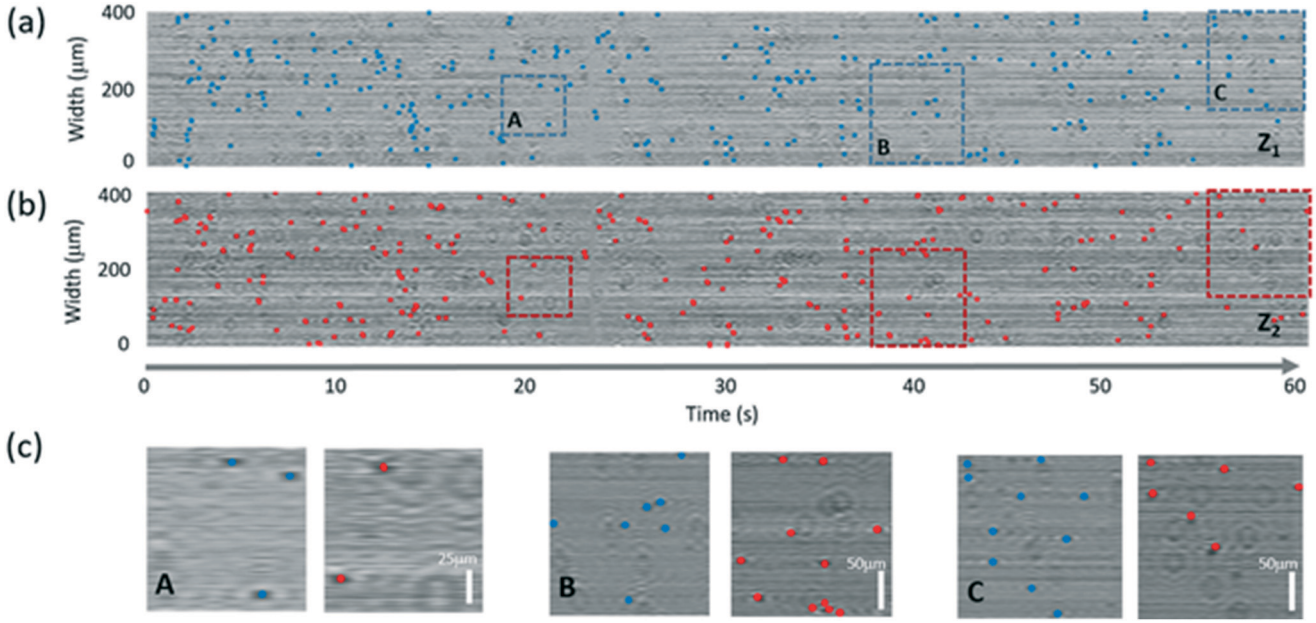

Fig. 5 Volumetric cell counting. (a and b) Count of RBCs flowing at two different heights inside the microfluidic channel (z_1 = −122.5 μm and z_2 = 50 μm). (c) Zoomed-in view of the dashed areas in (a) and (b).

Fig. 5(a) and (b) show segments of the numerical reconstructions of the synthetic hologram (corresponding to the first half of the STDH shown in Fig. 2(a)) after propagation at two axial positions, z_1 = −122.5 μm and z_2 = 50 μm from the hologram plane, respectively. In Fig. 5, the blue and red spots highlight the centroid locations of the RBCs counted by observing the planes z_1 and z_2, respectively. From each of these images, the presence of refocused samples where the centroid is estimated, along with the diffraction pattern from out-of-focus cells, is obvious. With respect to the intense and sharp spot of the former type of contribution, the latter constitutes a weak background signal and does not affect the y–t tracking (see Fig. 5(c)). Hence, in each plane of the volume, we locate and count the sole RBCs that are in focus. The final density of the RBCs was estimated to be 531 300 cells per ml. This is in good agreement with the expected dilution of 500 000 cells per ml (see the ESI†).

The recovery of out-of-focus information is essential for volumetric imaging. Notably, even if the diffraction patterns of out-of-focus objects can be seen on the acquisition plane, they are tricky to count and an accurate volumetric estimation is not possible. This is shown in Fig. 6, where blue spots indicate the RBCs tracked by STDH inspection, while red spots indicate the RBCs found only in positions different from the acquisition plane. The comparison between the results obtained with and without numerical propagation highlights the ability of holographic refocusing to recover the out-of-focus signal even in cases of low signal-to-noise ratios (SNRs) (see Fig. 5(b)).

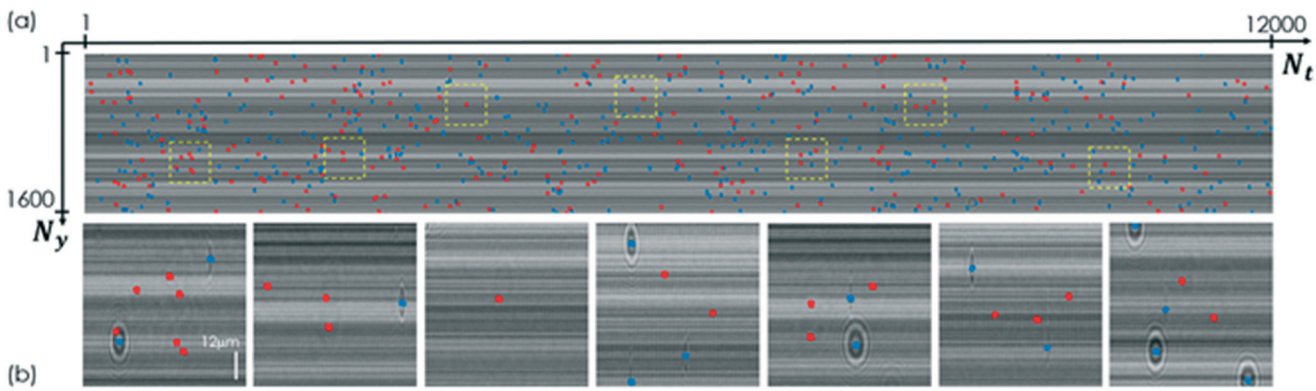

Fig. 6 Volumetric counting is achievable, thanks to holographic flexible focusing. (a) STDH with blue and red spots highlighting the centroid locations obtained by inspecting respectively the hologram plane and other planes after STDH propagation. (b) Enlarged details, corresponding to the yellow dashed boxes in (a). RBCs exhibiting a very weak diffraction signal in the acquisition plane are still counted since each cell is tracked and counted at its own best focus axial position.

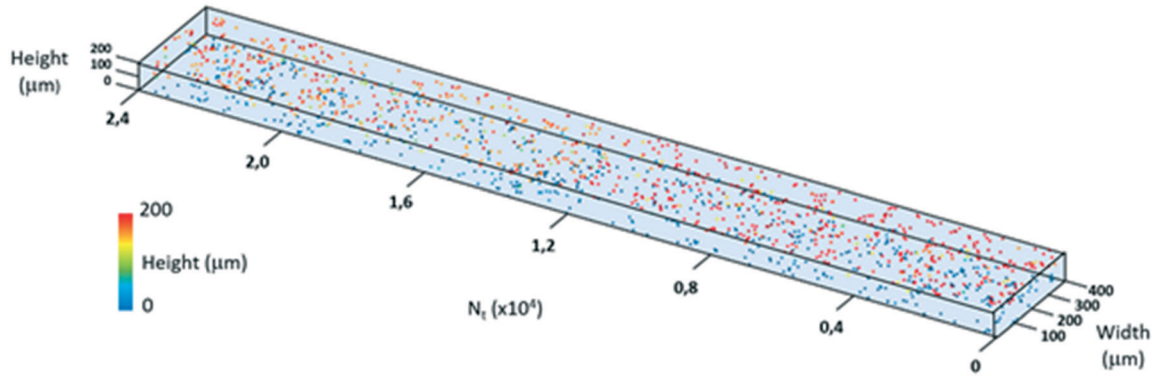

Fig. 7 3D tracking of the RBCs counted in the first 2.4×10^4 frames. Each point has a different color depending on the cell height inside the channel.

Due to the non-ideal sampling conditions, autofocusing of the whole synthetic hologram could not be, in principle, very accurate for cell localization along the z direction. Nevertheless, since the diffraction pattern is well sampled along the y dimension, an autofocusing algorithm can be applied, which measures the contrast, as a function of z, across one single line $t = t_c$ of the STDH (determined by the centroid position (y_c, t_c)).[29] Thus, 3D tracking is feasible for all the flowing cells.

Once the centroid location is determined, the axial position can be evaluated by measuring the Tamura coefficient as a function of the propagation distance. This is known to be a reliable contrast estimator, suitable for autofocusing in DH.[29] We measured the Tamura coefficient for each RBC over one single line crossing the centroid location and parallel to the y axis. Indeed, although the time undersampling impairs proper image formation in the best-focus plane, the diffraction pattern is well sampled in the y direction, so that the Tamura coefficient minimization turns out to be reliable in estimating the axial position for these RBCs from one line of their diffraction signature. The results of 3D tracking performed on the RBCs flowing through the channel for approximately five minutes are shown in Video 1† (a portion is shown in Fig. 7).

Conclusions

In summary, we have shown a LoC platform that allows for stable high-throughput volumetric imaging by a STDH modality. Stability is achieved through the adoption of embedded optical components on-chip in combination with a novel computational solution that compensates for problems related to a non-constant velocity distribution inside the channel.

This marks a necessary step in order to apply STDH in real cases of diagnostics, getting rid of the three main constraints typical of quantitative phase imaging: set-up complexity, limited field-of-view, and slow processing time.

Set-up complexity is avoided using a compact and low-cost HMS, with a wavefront division interferometer embedded directly on-chip.[23] This scheme circumvents the necessity for macroscopic optical components and bulky interferometers, standing as an off-the-shelf solution for off-axis STDH microscopy. Taking advantage of the flow of the sample, the spatio-temporal acquisition modality yields a substantially unlimited field-of-view and stores all volumetric data in a single continuous hologram. One single synthetic hologram representing the whole data of a microfluidic experiment can be propagated in a single, fast reconstruction process. This key feature drastically lowers the processing time, which represents a bottleneck for high-throughput acquisitions.

This problem has been addressed in the literature mainly by developing stitching algorithms, which put many holograms together in order to reduce the number of operations required for data recovery. Standard holographic acquisition, indeed, would require the calculation of two fast Fourier transforms for each image, which could require a negligible amount of time under normal conditions, but becomes cumbersome for high-throughput imaging. While different stitching algorithms have been proposed, they still require a finite processing time and specific experimental conditions. In STDH, on the other hand, the problem is solved *a priori* from the hardware rather than software point of view. Thus, only two FFTs are required to process the Fourier spectrum of the synthetic hologram, *i.e.* the representation of the entire experiment. This system is highly scalable since adding one more frame to the hologram dataset only increases the number of pixels to be processed (N_y), leaving the number of FFTs unchanged.

Moreover, different from other approaches that require very high performance hardware, here, a high throughput is obtainable using low-cost components, *e.g.* a LSA instead of a 2D CCD camera or a CMOS camera, in order to have a very high frame rate.

References

1 G. M. Whitesides, *Nature*, 2006, **442**, 368–373.
2 P. Yager, T. Edwards, E. Fu, K. Helton, K. Nelson, M. R. Tam and B. H. Weigl, *Nature*, 2006, **442**, 412–418.
3 F. Merola, P. Memmolo, L. Miccio, V. Bianco, M. Paturzo and P. Ferraro, *Proc. IEEE*, 2015, **103**(2), 192–204.
4 J. Wu, G. Zheng and L. M. Lee, *Lab Chip*, 2012, **12**, 3566–3575.

5 V. Bianco, M. Paturzo and P. Ferraro, *Opt. Express*, 2014, **22**(19), 22328–22339.
6 T.-W. Su, L. Xue and A. Ozcan, *Proc. Natl. Acad. Sci. U. S. A.*, 2012, **109**(40), 16018–16022.
7 S. A. Arpali, C. Arpali, A. F. Coskun, H. Chiang and A. Ozcan, *Lab Chip*, 2012, **12**(23), 4968–4971.
8 V. Bianco, M. Paturzo, V. Marchesano, I. Gallotta, E. Di Schiavi and P. Ferraro, *Lab Chip*, 2015, **15**(9), 2117–2124.
9 X. Heng, D. Erickson, L. R. Baugh, Z. Yaqoob, P. W. Sternberg, D. Psaltis and C. Yanga, *Lab Chip*, 2006, **6**, 1274–1276.
10 D. Vercruysse, A. Dusa, R. Stahl, G. Vanmeerbeeck, K. de Wijs, C. Liu, D. Prodanov, P. Peumans and L. Lagae, *Lab Chip*, 2015, **15**(4), 1123–1132.
11 W. Tsung-Feng, Y. T. Minghung, H. Yuanyuan, C. Yu-Jui, L. Y.-S. Eason and L. Yu-Hwa, *Lab Chip*, 2014, **14**, 3341–3348.
12 N. C. Pégard, M. L. Toth, M. Driscoll and J. W. Fleisher, *Lab Chip*, 2014, **14**, 4447–4450.
13 S. Fusco, P. Memmolo, L. Miccio, F. Merola, M. Mugnano, A. Paciello, P. Ferraro and P. A. Netti, *RSC Adv.*, 2016, **6**, 24245–24249.
14 A. Calabuig, M. Mugnano, L. Miccio, S. Grilli and P. Ferraro, *J. Biophotonics*, 2016, 1–9, DOI: 10.1002/jbio.201500340.
15 J. Yoon, K. Kim, H. Park, C. Choi, S. Jang and Y. Park, *Biomed. Opt. Express*, 2015, **6**(10), 3865–3875.
16 G. Di Caprio, A. El Mallahi, P. Ferraro, R. Dale, G. Coppola, B. Dale, G. Coppola and F. Dubois, *Biomed. Opt. Express*, 2014, **5**(3), 690–700.
17 W. M. Ash III, L. Krzewina and M. K. Kim, *Appl. Opt.*, 2009, **48**(34), H144–H152.
18 W. Xu, M. H. Jericho, I. A. Meinertzhagen and H. J. Kreuzer, *Proc. Natl. Acad. Sci. U. S. A.*, 2001, **98**, 11301–11305.
19 O. Mudanyali, D. Tseng, C. Oh, S. O. Isikman, I. Sencan, W. Bishara, C. Oztoprak, S. Seo, B. Khademhosseini and A. Ozcan, *Lab Chip*, 2010, **10**, 1417–1428.
20 G. R. Fienup, *Appl. Opt.*, 1989, **21**(15), 2758–2769.
21 W. Bishara, H. Zhu and A. Ozcan, *Opt. Express*, 2010, **18**(26), 27499–27510.
22 T. Latychevskaia and H. W. Fink, *Phys. Rev. Lett.*, 2007, **98**, 233901.
23 V. Bianco, B. Mandracchia, V. Marchesano, V. Pagliarulo, F. Olivieri, S. Coppola, M. Paturzo and P. Ferraro, Endowing a plain fluidic chip with micro-optics: a holographic microscope slide, *Light: Sci. Appl.*, 2017, DOI: 10.1038/lsa.2017.55, accepted article preview.
24 H. Bruus, *Governing Equations in Microfluidics. Microscale Acoustofluidics*, RSC Publishing, 2014, ch. 1, pp. 1–28, DOI: 10.1039/9781849737067-00001, eISBN:978-1-84973-706-7.
25 V. Vespini, S. Coppola, M. Todino, M. Paturzo, V. Bianco, S. Grilli and P. Ferraro, *Lab Chip*, 2016, **16**, 326–333.
26 https://www.ptgrey.com/frame-rate-vs-resolution-roi.
27 https://www.thorlabs.com/navigation.cfm?guide_id=2025.
28 M. K. Kim, Principles and techniques of digital holographic microscopy, *SPIE Rev.*, 2010, **1**, 1–50.
29 P. Memmolo, L. Miccio, M. Paturzo, G. Di Caprio, G. Coppola, P. A. Netti and P. Ferraro, Recent advances in holographic 3D particle tracking, *Adv. Opt. Photonics*, 2015, **7**, 713–755.

